

Exploring the giant dynamical Franz-Keldysh effect in massless Dirac materials

Youngjae Kim*

School of Physics, KIAS, Seoul 02455, Korea

(Dated: January 31, 2024)

The dynamical Franz-Keldysh effect, indicative of the transient light-matter interaction regime between quantum and classical realms, is widely recognized as an essential signature in wide bandgap condensed matter systems such as dielectrics. In this study, we applied the time-resolved transient absorption spectroscopy to investigate ultrafast optical responses in graphene, a zero-bandgap system. We observed in the gate-tuned graphene that the massless Dirac materials notably enhance intraband light-driven transitions, significantly leading to the giant dynamical Franz-Keldysh effect compared to the massive Dirac materials, a wide bandgap system. In addition, employing the angle-resolved spectroscopy, it is found that the perpendicular polarization orientation for the pump and the probe further pronounces the optical spectra to exhibit the complete fishbone structure, reflecting the unique pseudospin nature of Dirac cones. Our findings expand the establishment of emergent transient spectroscopy frameworks into not only zero-bandgap systems but also pseudospin-mediated quantum phenomena, moving beyond dielectrics.

In recent decades, the development of high-intensity and ultrashort laser pulses has opened new avenues for our understanding of ultrafast dynamics, enabling exploration at extreme time scales of 10 to 100 attoseconds ($1 \text{ as} = 10^{-18} \text{ s}$)[1–5]. These advances have not only facilitated ever faster temporal resolutions within a single cycle of optical fields but also significantly achieved the study of nonlinear responses and their properties[6, 7].

One of the central achievements is ultrafast transient absorption spectroscopy (TAS), which has emerged as a crucial technique for probing transient optical properties in various excited electronic systems. Initially originating in studies of atomic and molecular systems[7–9], TAS has been broadened to probe the characteristics of condensed matter systems: rapid dipole oscillations[10], controls of electric carriers[11–13], crystal orientations[14], and the dynamical Franz-Keldysh effect (DFKE)[14–21].

The DFKE becomes completely characterized in the transient regime between quantum and classical realms[20, 21], particularly when non-interacting wide bandgap systems, such as dielectrics, are exposed to intense and alternating external electric fields. This effect is mainly marked by distinct features[14, 19, 21–24]: real-time V-shaped phase oscillations, known as the fishbone structure induced by intraband transitions, and the redshift in their differential TAS. The redshift originates from field-induced modifications of the band structures, as interpreted in the Franz-Keldysh effect (FKE)[21, 25–28], leading to an increase in absorption spectra below the bandgap edge in the adiabatic limit.

Recent experimental and theoretical studies have expanded the understanding of the DFKE. For instance, an experimental studies on diamond have demonstrated the transient absorptions induced by intense pump pulses, also clearly explained by the first-principles calculations[18, 19]. Further theoretical works have explored the DFKE in many-body interacting systems. In multi-band charge transfer insulators within the time-

dependent density functional theory plus U, the DFKE is observed to be screened due to the strong screenings in many-body correlations[29]. Moreover, in pure Mott insulating phases computed by the time-dependent exact diagonalizations, nontrivial aspects of the DFKE are induced by the transitions of double occupancy[30]. However, the exploration of transient dynamics via TAS has been still predominantly confined to wide bandgap systems. Given these advancements, it is now timely to propose expanding the establishments of TAS to another avenue, unveiling emergent transient dynamics beyond the dielectrics.

On the other side, graphene, considered as an essential quantum material, exhibits a range of intriguing properties, from nonlinear optical effects[31–33] to topological[34–36] and superconducting[37, 38] phenomena. A key aspect of graphene is the presence of massless Dirac fermions, categorizing it as a zero-bandgap system. Considering this point, we focus on the gate-tuned graphene. The gate-tuning can modulate the chemical potential to control its optical responses where the interband transitions of Dirac cone become forbidden due to empty states above the chemical potential[39, 40] whereas the intraband transitions are still allowed. Although a gate-tuned graphene was previously suggested to exhibit the DFKE[41], deep demonstrations under the ultrafast TAS have been rarely studied, primarily because the FKE was rooted in dielectrics[4].

In this study, we demonstrate the time-resolved ultrafast TAS to investigate emergent optical responses and transient dynamics in gate-tuned graphene. We find that the signal of the DFKE evolves distinctively with chemical potential alterations. Moreover, angle-resolved polarization orientations for the pump and probe pulses reveal that the absorption responses vary with the angle. Eventually, perpendicular polarization orientation predominantly yields much more explicit DFKE signals, characterized by the fishbone structures and the redshifts,

reflecting the pseudospin nature of graphene.

In addition, comparing the massless and the massive Dirac materials under identical laser pulse conditions, we observe that the DFKE in the massless Dirac systems is significantly pronounced, by the enhanced intraband light-driven transitions[24] due to its massless electronic structures. Our findings propose that gate-tuned graphene would be an ideal platform for the emergent researches for the DFKE, extending the framework of transient spectroscopy into zero-bandgap and pseudospin-mediated quantum phenomena.

We employ the time-dependent equation of motion to elucidate the microscopic quantum mechanical light-matter interactions in Dirac materials[31], expressed as,

$$\partial/\partial\tau\rho_{\mathbf{k}}(\tau) = -i[H_{\mathbf{k}}(\tau), \rho_{\mathbf{k}}(\tau)] \quad (1)$$

Here, the density matrix $\rho_{\mathbf{k}}(\tau)$, defined within the Houston states describing the instantaneous electronic states at momentum $\mathbf{k}(\tau)$. The Hamiltonian $H_{\mathbf{k}}(\tau)$ is expanded from momenta \mathbf{K} and $-\mathbf{K}$ and can be described as $H_{\mathbf{k}}(\tau) = v_F\xi\bar{\sigma}_x k_x(\tau) + v_F\bar{\sigma}_y k_y(\tau)$, where $\bar{\sigma}_{x(y)}$ denotes the Pauli matrix. The Fermi velocity v_F in graphene is given in the energy unit of -13.88 eV, and ξ is the valley parameter for \mathbf{K} ($\xi = 1$) and $-\mathbf{K}$ ($\xi = -1$). The time-dependent momentum $\mathbf{k}(\tau) = \mathbf{k} - \mathbf{A}(\tau)/c$ is derived using the Peierls substitution, with the speed of light c and the vector potential $\mathbf{A}(\tau) \rightarrow \mathbf{A}_{pu}(\tau) + \mathbf{A}_{pr}(\tau - \tau_d)$: the pump and the probe pulses, respectively, as depicted in the Fig.1(a). The pump pulse is $\mathbf{A}_{pu}(\tau) = A_0 \cos(\omega_0\tau) \cos^2(\pi\tau/2\tau_0)\hat{\mathbf{x}}$ at $|\pi\tau/2\tau_0| < \pi/2$ and $\mathbf{A}_{pu}(\tau) = 0$ elsewhere. We adopt the ultrashort (a few cycles) NIR pump pulse with 27 fs of τ_0 and 0.55 eV of ω_0 , thus ~ 7 optical cycles are included in a single pulse packet. The probe pulse $\mathbf{A}_{pr}(\tau) = \lambda\delta(\tau)\hat{\mathbf{x}}$ with $\lambda = 0.001|v_F|$ for the linear response limit. The probe is polarized along the x-direction unless stated otherwise (also see the Fig.1(a)).

As depicted in Fig.1(b), the initial distribution of electrons is thermalized by the chemical potential μ , follows by $\rho_{\mathbf{k}}(\tau \rightarrow -\infty)_{n,m} = \delta_{n,m}(e^{(\varepsilon_{\mathbf{k},n}-\mu)/k_B T} + 1)^{-1}$, with temperature $T = 80$ K, the Boltzmann constant k_B , and the initial eigen energies $\varepsilon_{\mathbf{k},n}$. Therefore, the dynamics in Dirac cones vary with μ . At $\mu = 0$ in the charge neutral states, both inter- and intraband transitions contribute to the dynamics. When μ attains a finite value in the gate-tuned states, however, interband transitions below $\Delta = 2|\mu|$ become forbidden, while intraband transitions continue to occur. Fig.1(c) shows the temporal profile of the pump laser pulse applied to graphene, with the peak electric field strength $E_0 = 0.04$ V/Å of $\mathbf{E}_{pu}(\tau) = -(1/c)\partial\mathbf{A}_{pu}(\tau)/\partial\tau$. The bottom inset of Fig.1(c) displays the number of excited electrons as a function of μ . The number of excited electrons is $n_e(\tau) = 1/(2\pi)^2 \int d\mathbf{k}^2 [\rho_{\mathbf{k}}(\tau)_{n,n} - \rho_{\mathbf{k}}(\tau \rightarrow -\infty)_{n,n}]$ with n for the upper Dirac states. In case of charge neutral state, the electrons are significantly excited due to the

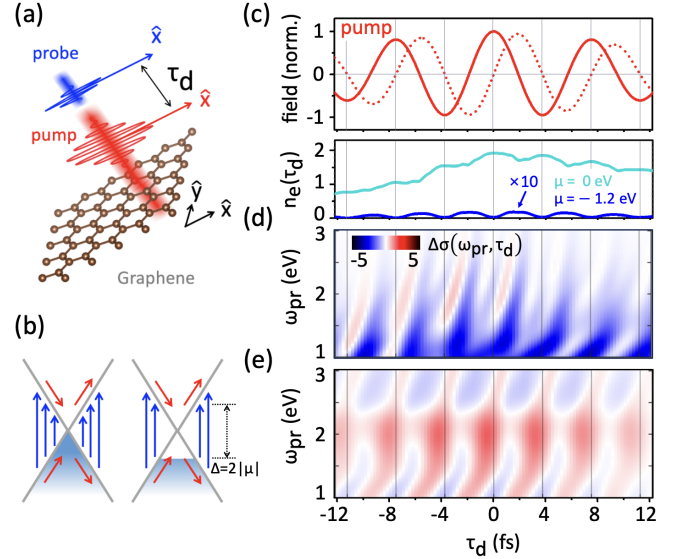


FIG. 1. The ultrafast TAS on gate-tuned graphene. (a), Schematics of the pump and probe spectroscopy for the TAS. The pump and the probe pulses are aligned with same direction, i.e., the x-direction. (b), Dirac cones with the chemical potential alternation, μ , which introduces $\Delta = 2|\mu|$. The red and blue arrows stand for optical transitions of the pump and the probe, respectively. (c), Normalized time-profile of the pump pulse. The peak electric field is $E_0 = 0.04$ V/Å. The solid and the dotted lines represent the vector potential and the electric field, respectively. The bottom inset shows the time-dependent excited electrons n_e in arbitrary unit, in cases of $\mu = 0$ eV and -1.2 eV. (d), (e), Calculated ultrafast TAS $\Delta\sigma(\omega_{pr}, \tau_d)$ for $\mu = 0$ eV (d) and -1.2 eV (e).

zero-bandgap structures of Dirac cone. In the gate-tuned states with $\mu = -1.2$ eV, however, direct optical excitations are not permissible so that n_e can be ignored, emphasizing the remaining intraband transitions. Thus, in the gate-tuned graphene, the pump pulse mostly contributes to the intraband transitions, and similarly, the interband transitions are mainly contributed from the probe pulse.

To investigate time-resolved TAS using transient optical conductivities, first we obtain the optical conductivities of initial states as,

$$\sigma_0(\omega_{pr}) = \Re[\mathbf{J}_{pr}(\omega_{pr})/\mathbf{E}_{pr}(\omega_{pr})] \quad (2)$$

Here, $\Re[\dots]$ extracts the real part in the [...]. The current density $\mathbf{J}_{pr}(\tau)$ is obtained from $\mathbf{J}_{pr}(\tau) = 1/(2\pi)^2 \int d\mathbf{k}^2 \text{tr}[\mathbf{j}_{\mathbf{k}}(\tau)\rho_{\mathbf{k}}(\tau)]$, with the current operator $\mathbf{j}_{\mathbf{k}}(\tau) = -\partial H_{\mathbf{k}}(\tau)/\partial\mathbf{A}(\tau)$ and $\mathbf{k}(\tau) = \mathbf{k} - \mathbf{A}(\tau)/c$ for $\mathbf{A}(\tau) = \mathbf{A}_{pr}(\tau)$. These values are transformed into frequency space as $\mathbf{J}_{pr}(\omega) = \int d\tau e^{-\eta\tau+i\omega\tau}\mathbf{J}_{pr}(\tau)$ and $\mathbf{E}_{pr}(\omega) = \int d\tau e^{-\eta\tau+i\omega\tau}\mathbf{E}_{pr}(\tau)$, with $\eta = 0.3$ eV as a smearing parameter.

Subsequently, we calculate transient conductivities by $\mathbf{J}_{tr}(\tau, \tau_d) = \mathbf{J}_{pu+pr}(\tau, \tau_d) - \mathbf{J}_{pu}(\tau)$. The $\mathbf{J}_{pu+pr}(\tau, \tau_d)$

should be the current densities when the Dirac hamiltonian $H_{\mathbf{k}(\tau)}$ is evolved by the vector potential $\mathbf{k}(\tau) = \mathbf{k} - \mathbf{A}(\tau)/c$ for $\mathbf{A}(\tau) = \mathbf{A}_{pu}(\tau) + \mathbf{A}_{pr}(\tau - \tau_d)$ and similarly, $\mathbf{J}_{pu}(\tau)$ under $H_{\mathbf{k}(\tau)}$ for $\mathbf{A}(\tau) = \mathbf{A}_{pu}(\tau)$. Finally, the difference spectra of TAS, which we shall call TAS hereafter, is practically obtained as[14],

$$\Delta\sigma(\omega_{pr}, \tau_d) = \Re[\mathbf{J}_{tr}(\omega_{pr}, \tau_d)/\mathbf{E}_{pr}(\omega_{pr}, \tau_d)] - \sigma_0(\omega_{pr}) \quad (3)$$

Fig.1(d) and (e) depict TAS results to compare charge neutral states ($\mu = 0$) with gate-tuned states ($\mu = -1.2$ eV). In the charge neutral states (Fig.1(d)), the TAS shows negative signs continuously across the entire spectra, a consequence of Pauli blocking by excited electrons and holes, as indicated in the inset of Fig.1(c). In contrast, Fig.1(e) shows that the TAS of gate-tuned graphene exhibits positive signs at $\omega_{pr} < 2.4$ eV where the $\Delta = 2|\mu| = 2.4$ eV for $\mu = -1.2$ eV. Above 2.4 eV, the TAS shows dominant negative signals. These results correspond to the redshifts, one of the signatures of the DFKE[19, 21]. However, the fishbone structure, another signature of the DFKE, are not completely observed at this stage, despite the explicit presence of time-dependent phase oscillations with frequency of $2\omega_0$. Thus, the TAS in Fig.1(e) provides the incomplete signal of the DFKE. We note that time-resolved spectroscopy on sub-laser-cycle electron dynamics necessitates $\omega_{pr} \gg \omega_0$, limiting our discussion to low frequency range at $\omega_{pr} < 1$ eV.

In Fig.2, we further demonstrate how the TAS $\Delta\sigma(\omega_{pr}, \tau_d)$ changes when the polarization of the probe pulse is rotated to align along $\hat{\mathbf{x}}'$, i.e., $\hat{\mathbf{x}}' = \cos\theta_{pr}\hat{\mathbf{x}} + \sin\theta_{pr}\hat{\mathbf{y}}$. Consequently, the probe pulse is set as $\mathbf{A}_{pr}(\tau) = \lambda\delta(\tau)\hat{\mathbf{x}}'$, while the pump pulse $\mathbf{A}_{pu}(\tau)$ remains as $\mathbf{A}_{pu}(\tau) \parallel \hat{\mathbf{x}}$, as shown in Fig.2(a). We now investigate the $\Delta\sigma(\omega_{pr}, \tau_d)$ along $\hat{\mathbf{x}}'$. As illustrated in Fig.2(b-d), it is notable that the observed spectra depend on the angle θ_{pr} , even under the same pump pulse characteristics. Interestingly, at $\theta_{pr} = \pi/2$ (Fig.2(d)), the spectra distinctly reveal the missing feature of the DFKE in Fig.1, that is, the fishbone structure, as indicated by the dotted line. This suggests that an unusual orientation, $\theta_{pr} = \pi/2$, between the pump and probe is crucial in the case of massless Dirac systems to measure the complete signal of the DFKE.

To identify the rotation-dependent behaviors in the spectra, we present the time-averaged spectra, defined over a single period of the pump pulse, for different μ values in Fig.2(e-f). The rise and the decay behaviors of the spectra below and above $\Delta (= 2|\mu|)$, respectively, are clearly observed for various θ_{pr} values, with both $\mu = -0.8$ eV and -1.2 eV. These behaviors coincide with the DFKE in wide bandgap systems and can be interpreted as the effect of the FKE[21, 42]. Notably, the decay behaviors of the spectra at $\omega_{pr} > \Delta$ exhibit a more dramatic response with respect to θ_{pr} compared to the rise

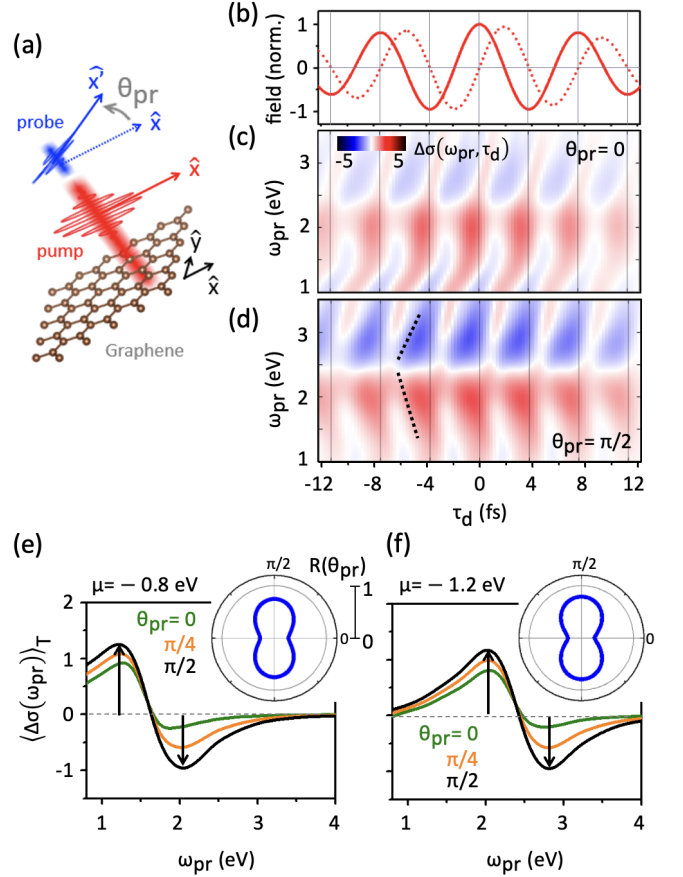


FIG. 2. Calculated TAS on the gate-tuned graphene with angle-resolved polarization orientations between the pump and the probe pulses. (a), Schematics of the angle-resolved geometry. The polarization of the probe pulse, $\hat{\mathbf{x}}'$, is rotated by θ_{pr} with respect to the x-direction. (b), Normalized time-profile of the pump pulse with $E_0 = 0.04V\text{\AA}$. (c), (d), Calculated TAS at the $\theta_{pr} = 0$ (c) and the $\theta_{pr} = \pi/2$ (d). The dotted line in the (d) is drawn as the guide for eyes for the fishbone structure. (e), (f), Calculated time-averaged TAS, $\langle \Delta\sigma(\omega_{pr}) \rangle_T = 1/T_0 \int_{-T_0/2}^{T_0/2} d\tau_d \Delta\sigma(\omega_{pr}, \tau_d)$ where time-period of pump pulse, $T_0 = 2\pi/\omega_0$. The time-averaged TAS in cases of $\mu = -0.8$ eV (e) and $\mu = -1.2$ eV (f) as a function of θ_{pr} . In the polar plot insets show the symmetrmetry in the spectra defined by the relative signal strength $R(\theta_{pr}) = |R_n(\theta_{pr})|/R_p(\theta_{pr})$. The $R_{p(n)}$ denotes for highest positive (lowest negative) value of $\langle \Delta\sigma(\omega_{pr}) \rangle_T$, i.e., $R_{p(n)}(\theta_{pr}) = \max(\min)[\langle \Delta\sigma(\omega_{pr}) \rangle_T]$ at given θ_{pr} , as indicated by the black arrows in (e), (f).

behaviors at $\omega_{pr} < \Delta$, which is more clearly visible in the insets of polar plots in Fig.2(e), (f). In the inset, it is also evident that $\theta_{pr} = \pi/2$ is a critical point where the lowest negative value of $\langle \Delta\sigma(\omega_{pr}) \rangle_T$ is comparable to its highest positive value. This indicates that the entire spectra become symmetric forms around Δ , corresponding to pronounced intraband light-driven transitions completely detectable by the TAS.

To gain a deeper understanding of the physics underlying

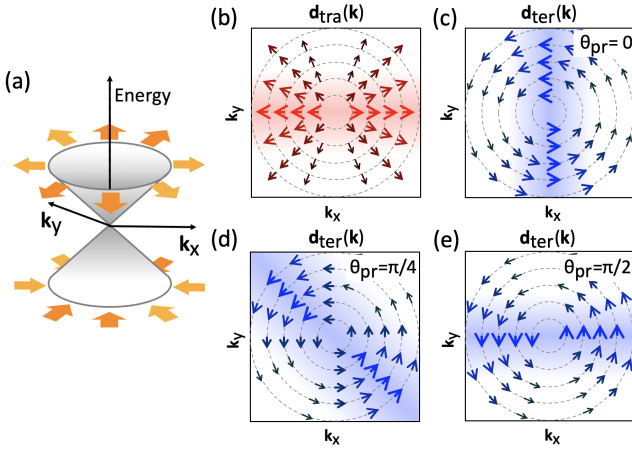


FIG. 3. Quantum pseudospin textures and related transition momentum matrix. (a), In-plane arranged pseudospin textures (yellow arrows) in a Dirac cone. (b-e), Normalized momentum matrix of a Dirac cone displayed in the momentum space. Note, the dashed concentric circles represent the isoenergy lines for Dirac cone centered at the Dirac point. Size of arrows and colors indicate the strength of momentum matrix under given laser field direction. Each arrow indicates the direction of momentum matrix. (b), Intraband momentum matrix $\mathbf{d}_{tra}(\mathbf{k})$ under the x-polarized laser field, i.e., the pump pulse. (c-e), Interband momentum matrix $\mathbf{d}_{ter}(\mathbf{k})$ under the laser field, i.e., the probe pulse, under various θ_{pr} : 0 (c), $\pi/4$ (d), and $\pi/2$ (e).

ing massless Dirac materials, we examine the unique electronic structures of the Dirac cone, as depicted in Fig.3. In graphene, due to the identical sub-lattice degree of freedom, the Dirac cone can be expressed by the pseudospin notation using the Pauli matrix $\bar{\sigma}$ (see Fig.3(a)). Consequently, the momentum matrix can be formulated as $\mathbf{A} \cdot \bar{\sigma}$. The intraband momentum matrix $\mathbf{d}_{tra}(\mathbf{k})$ and the interband momentum matrix $\mathbf{d}_{ter}(\mathbf{k})$ are represented as $\mathbf{d}_{tra}(\mathbf{k}) = \langle \pm \mathbf{k} | \mathbf{A} \cdot \bar{\sigma} | \pm \mathbf{k} \rangle$ and $\mathbf{d}_{ter}(\mathbf{k}) = \langle \pm \mathbf{k} | \mathbf{A} \cdot \bar{\sigma} | \mp \mathbf{k} \rangle$, respectively, where $|n\mathbf{k}\rangle$ corresponds to the eigenstates of the Dirac cone.

When a x-polarized laser is applied, the \mathbf{d}_{tra} predominantly arises from the k_x sectors of the Dirac cone, as illustrated in Fig.3(b), which corresponds to the pump pulse in our study. In contrast, \mathbf{d}_{ter} behaves differently due to its pseudospin properties. As shown in Fig.3(c), when a x-polarized laser is applied, \mathbf{d}_{ter} aligns perpendicularly along the k_y sectors, which mainly corresponds to the probe pulse in our study. In this case, the pump and probe pulses do not fully overlap in momentum space. This explains why incomplete spectra of the DFKE are observed in parallel polarization orientations between the pump and probe pulses, as shown in Fig.1 and Fig.2. However, as depicted in Fig.3(d) and (e), rotating the orientation of the probe pulse results in complete spectra, as the two momentum matrices begin to overlap with increasing θ_{pr} . Notably, the $\theta_{pr} = \pi/2$ results in the full overlap and yields complete spectra of the DFKE, as ev-

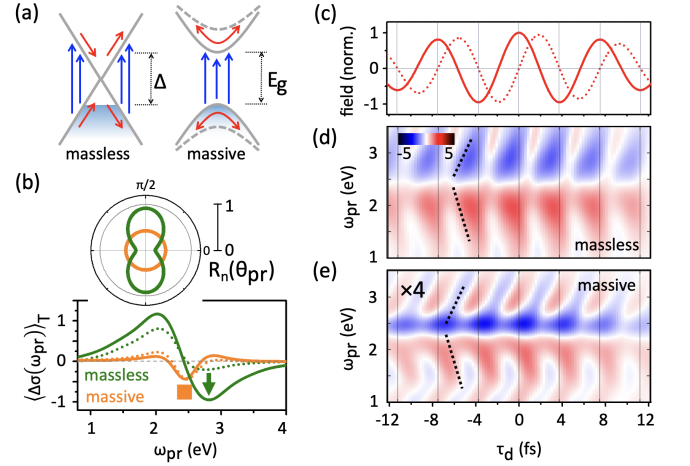


FIG. 4. The giant DFKE measured in the massless Dirac materials and a comparison between the massless and the massive Dirac materials. (a), Schematics of dynamics in massless Dirac materials with $\mu = -1.2$ eV, $\Delta = 2|\mu|$ and the massive Dirac materials with band gap E_g of 2.4 eV. (b), The time-averaged TAS of massive and massless Dirac materials. The solid and dotted lines represent the results of $\theta_{pr} = \pi/2$ and $\theta_{pr} = 0$, respectively. The box and arrow symbols indicate the minimum value of each TAS. The polar plot inset shows θ_{pr} -dependent lowest negative value of spectra, $|R_n(\theta_{pr})|$, ($R_n(\theta_{pr}) = \min[\langle \Delta \sigma(\omega_{pr}) \rangle_T]$), same definition in the Fig.2, for the massless and the massive Dirac materials. (c), Time-profile of the pump pulse. $E_0 = 0.04V \text{ \AA}$. (d),(e) Calculated TAS for the massless Dirac materials with $\theta_{pr} = \pi/2$ (d) and the massive Dirac materials with $\theta_{pr} = 0$. Note, the (d) is zoomed-in image about four times.

idenced in Fig.2, reflecting the critical role of pseudospin nature in massless Dirac systems.

Finally, Fig.4 presents a comparative analysis of TAS between graphene and wide-bandgap systems, examining both massless and massive Dirac materials. To incorporate massive Dirac materials, we introduce a mass parameter E_g into the Dirac Hamiltonian used in Eq.(1), by $H_{\mathbf{k}(\tau)} \rightarrow H_{\mathbf{k}(\tau)} + E_g/2\bar{\sigma}_z$. This allows us to compare dynamics between massless Dirac materials with $\mu = -1.2$ eV ($\Delta = 2.4$ eV) and massive Dirac materials with $E_g = 2.4$ eV under identical laser conditions, as shown in Fig.4(a).

In Fig.4(b), we observe distinct behaviors in the time-averaged TAS for both systems. We emphasize two remarkable aspects in this figure. First, in massless Dirac materials, the spectra at $\omega_{pr} < \Delta$ exhibit pronounced redshifts, overwhelming those in massive Dirac systems across all θ_{pr} values. This originates from the high velocity of massless Dirac materials, enhancing intraband light-induced transitions[24] compared to massive systems. Second, in massless Dirac materials, a dramatic decrease in negative spectra at $\omega_{pr} > \Delta$ is observed as the θ_{pr} increases, as indicated by the arrow in Fig.4(b). In contrast, the massive Dirac systems show no significant

change under varying θ_{pr} , as shown by the box symbol in Fig.4(b). The polar plot inset of Fig.4(b) clearly illustrates this phenomenon. In the inset, the lowest negative spectra in the massless Dirac materials varying with θ_{pr} , and pronounced at $\theta_{pr} = \pi/2$. This demonstrates the pseudospin nature of the Dirac cone, which exhibits in-plane pseudospins in the entire momentum space, as depicted in Fig3(a). In contrast, massive Dirac systems show constant responses regardless of θ_{pr} , due to their pseudospins aligning along the z-direction at the bandgap edge, lacking in-plane directional properties.

Additionally, in Fig4(b), even though the gap parameters are equally set at $\Delta = E_g = 2.4$ eV, the points where the spectral signs change differ between the two systems. In massless Dirac systems, this sign change occurs exactly at $\omega_{pr} = \Delta$, while in massive systems, it appears slightly below E_g . This phenomenon in massive systems is attributed to the light-induced blueshift at the bandgap edge typically in dielectrics[4, 43]—as represented by the massive Dirac systems in our study. The ponderomotive energy from the intraband transitions in these systems always causes the bandgap to be widen, resulting in an increased effective bandgap, as shown in Fig.4(a) (see the solid and the dashed lines in the massive Dirac systems). This leads to markedly enhanced optical transparency, observed as a strong negative signal, around the bandgap edge at $\omega_{pr} \sim E_g$. In contrast, the massless Dirac system, when gate-tuned, is essentially a gapless material featuring a metallic Fermi surface, and thus does not exhibit a light-induced blueshift.

In our last discussion, Fig.4(c,e) display the TAS results for both systems, clearly illustrating the DFKE, characterized by fishbone structures and redshifts. Although the TAS from the massive systems (Fig.4(e)) conventionally represent the DFKE, we note that the TAS from massless systems (Fig.4(d)) shows much pronounced DFKE features, suggesting graphene as an ideal material for studying the DFKE.

In summary, our study on time-resolved ultrafast TAS in graphene reveals distinct optical responses and the evolution of the DFKE with gate-tuning. Angle-resolved polarization orientations for the pump and probe pulses significantly affect the TAS signals, especially when aligned perpendicularly, identifying the pseudospin nature of Dirac cones. A comparative analysis between massless and massive Dirac materials under identical laser conditions shows the pronounced DFKE in massless systems, attributable to high intraband transitions of the Dirac cones. These findings suggest that gate-tuned graphene is an ideal platform for DFKE studies, extending the TAS framework into zero-bandgap systems and offering insights into the real-time quantum pseudospin dynamics, thereby advancing the potential realm of ultrafast spectroscopy throughout condensed matter physics.

ACKNOWLEDGEMENT

The authors thank the computational support from the Center for Advanced Computation (CAC) at Korea Institute for Advanced Study (KIAS). In this study, Y.K. supported by a KIAS Individual Grant (PG088601) at Korea Institute for Advanced Study (KIAS).

* Corresponding author: ykim.email@gmail.com

-
- [1] R. Kienberger, E. Goulielmakis, M. Uiberacker, A. Baltuska, V. Yakovlev, F. Bammer, A. Scrinzi, Th. Westerwalbesloh, U. Kleineberg, U. Heinzmann, M. Drescher, and F. Krausz, *Nature* **427**, 817–821 (2004).
 - [2] A. L. Cavalieri, N. Müller, Th. Uphues, V. S. Yakovlev, A. Baltuska, B. Horvath, B. Schmidt, L. Blümel, R. Holzwarth, S. Hendel, M. Drescher, U. Kleineberg, P. M. Echenique, R. Kienberger, F. Krausz, and U. Heinzmann, *Nature* **449**, 1029–1032 (2007).
 - [3] F. Krausz and M. Ivanov, *Rev. Mod. Phys.* **81**, 163 (2009).
 - [4] S. Yu. Kruchinin, F. Krausz, V. S. Yakovlev, *Rev. of Mod. Phys.* **90**, (2018).
 - [5] M. Lucchini, S. A. Sato, G. D. Lucarelli, B. Moio, G. Inzani, R. Borrego-Varillas, F. Frassetto, L. Poletto, H. Hübener, U. D. Giovannini, A. Rubio, and M. Nisoli, *Nat. Commun.* **12**, 1021 (2021).
 - [6] M. Holler, F. Schapper, L. Gallmann, and U. Keller, *Phys. Rev. Lett.* **106**, 123601 (2011).
 - [7] E. Goulielmakis, Z.-H. Loh, A. Wirth, R. Santra, N. Rohringer, V.S. Yakovlev, S. Zherebtsov, T. Pfeifer, A. M. Azzeer, M. F. Kling, S. R. Leone, and F. Krausz, *Nature* **466**, 739–743 (2010).
 - [8] M. Chini, B. Zhao, H. Wang, Y. Cheng, S. X. Hu, and Z. Chang, *Phys. Rev. Lett.* **109**, 073601 (2012).
 - [9] L. Drescher, M. J. J. Vrakking, and J. Mikosch, *J. Phys. B: At. Mol. Opt. Phys.* **53** 164005, 9 (2020).
 - [10] H. Mashiko, K. Oguri, T. Yamaguchi, A. Suda, and H. Gotoh *Nat. Phys.* **12**, 741–745 (2016).
 - [11] M. Schultze, K. Ramasesha, C.D. Pemmaraju, S.A. Sato, D. Whitmore, A. Gandman, J. S. Prell, L. J. Borja, D. Prendergast, K. Yabana, D. M. Neumark, S. R. Leone, *Science* **346**, 1348-1352 (2014).
 - [12] M. Zürch, H.-T. Chang, L. J. Borja, P. M. Kraus, S. K. Cushing, A. Gandman, C. J. Kaplan, M. H. Oh, J. S. Prell, D. Prendergast, C. D. Pemmaraju, D. M. Neumark, and S. R. Leone, *Nat. Commun.* **8**, 15734 (2017).
 - [13] F. Schlaepfer, M. Lucchini, S. A. Sato, M. Volkov, L. Kasmi, N. Hartmann, A. Rubio, L. Gallmann, U. Keller, *Nat. Phys.* **14**, 560–564 (2018).
 - [14] S. A. Sato, H. Hübener, U. D. Giovannini, and A. Rubio, *Appl. Sci.* **8**(10), 1777 (2018).
 - [15] Y. Yacoby, *Phys. Rev.* **169**, 610–619 (1968).
 - [16] A. P. Jauho and K. Johnsen, *Phys. Rev. Lett.* **76**, 4576–4579 (1996).
 - [17] M. Du, C. Liu, Y. Zheng, Z. Zeng, and R. Li, *Phys. Rev. A* **100**, 043840 (2019).
 - [18] M. Lucchini, S. A. Sato, A. Ludwig, J. Herrmann, M. Volkov, L. Kasmi, Y. Shinohara, K. Yabana, L. Gall-

- mann, U. Keller, *Science* **353**, 6302 (2016).
- [19] M. Lucchini, S. A. Sato, F. Schlaepfer, K. Yabana, L. Gallmann, A. Rubio, and U. Keller, *J. Phys.: Photonics* **2** 025001 (2020).
- [20] F. Novelli, D. Fausti, F. Giusti, F. Parmigiani, and M. Hoffmann, *Sci. Rep.* **3**, 1227 (2013).
- [21] T. Otobe, Y. Shinohara, S. A. Sato, and K. Yabana, *Phys. Rev. B* **93**, 045124 (2016).
- [22] F. Dong and J. Liu, *Phys. Rev. A* **106**, 063107 (2022).
- [23] A. Srivastava and J. Kono, Postconference Digest Quantum Electronics and Laser Science, 2003. QELS., Baltimore, MD, USA, 2003, pp. 2 pp.-, doi: 10.1109/QELS.2003.238340.
- [24] A. Picón, L. Plaja and J. Biegert, *New J. Phys.* **21**, 043029, (2019).
- [25] W. Franz, *Z. Naturforschung* **13a**, 484 (1958).
- [26] L. Keldysh, *J. Exptl. Theoret. Phys.* **33**, 994 (1957).
- [27] R. E. Nahory and J. L. Shay, *Phys. Rev. Lett.* **21**, 1569 (1968).
- [28] K. Tharmalingam, *Phys. Rev.* **130**, 2204 (1963).
- [29] N. Tancogne-Dejean, M. A. Sentef, and A. Rubio, *Phys. Rev. B* **102**, 115106 (2020).
- [30] Y. Kim, *Phys. Rev. B* **108**, 035122 (2023).
- [31] S. A. Sato, H. Hirori, Y. Sanari, Y. Kanemitsu, and A. Rubio, *Phys. Rev. B* **103**, L041408 (2021).
- [32] N. Yoshikawa, T. Tamaya, and K. Tanaka, *Science* **356**, 736 (2017).
- [33] T. Jiang, D. Huang, J. Cheng, X. Fan, Z. Zhang, Y. Shan, Y. Yi, Y. Dai, L. Shi, K. Liu, C. Zeng, J. Zi, J. E. Sipe, Y.-R. Shen, W.-T. Liu, S. Wu, *Nat. Photon.* **12**, 430–436 (2018).
- [34] K. W. Kim, H. Kwon, and K. Park, *Phys. Rev. B* **99**, 115136 (2019).
- [35] J. W. McIver, B. Schulte, F.-U. Stein, T. Matsuyama, G. Jotzu, G. Meier, and A. Cavalleri, *Nat. Phys.* **16**, 38–41 (2020).
- [36] T. Oka and H. Aoki, *Phys. Rev. B* **79**, 081406(R), (2009).
- [37] E. Y. Andrei and A. H. MacDonald, *Nat. Mater.* **19**, 1265–1275 (2020).
- [38] Y. Cao, V. Fatemi, A. Demir, S. Fang, S. L. Tomarken, J. Y. Luo, J. D. Sanchez-Yamagishi, K. Watanabe, T. Taniguchi, E. Kaxiras, R. C. Ashoori, and P. Jarillo-Herrero, *Nature* **556**, 80–84 (2018).
- [39] J. Horng, C.-F. Chen, B. Geng, C. Girit, Y. Zhang, Z. Hao, H. A. Bechtel, M. Martin, A. Zettl, M. F. Crommie, Y. R. Shen, and F. Wang, *Phys. Rev. B* **83**, 165113 (2011).
- [40] Z. Q. Li, E. A. Henriksen, Z. Jiang, Z. Hao, M. C. Martin, P. Kim, H. L. Stormer, and D. N. Basov, *Nat. Phys.* **4**, 532–535 (2008).
- [41] Y. Zhou and M. W. Wu, *Phys. Rev. B* **83**, 245436 (2011).
- [42] B. O. Seraphin and N. Bottka, *Phys. Rev.* **139**, A560, (1965).
- [43] A. Srivastava, R. Srivastava, J. Wang, and J. Kono, *Phys. Rev. Lett.* **93**, 157401, (2004).